Probing confined fields with single molecules and *vice versa*

B. SICK*, B. HECHT*, U. P. WILD* & L. NOVOTNY†

Physical Chemistry Laboratory, Swiss Federal Institute of Technology, ETH-Zentrum, CH-8092 Zürich, Switzerland

†*The Institute of Optics, University of Rochester, Rochester, NY 14627, U.S.A.*

Summary

Single dye molecules are used as local probes to map the spatial distribution of the squared electric field components in the focus of a high numerical aperture lens. Simulated field distributions are quantitatively verified by experimentally obtained fluorescence excitation maps. We show that annular illumination can be used to engineer the field distribution in the focus at a dielectric/air interface such that electric field components in all directions acquire comparable magnitudes. The 3D orientation of molecular absorption dipoles can be determined by comparing measured to simulated image patterns. The presence of longitudinal electric field components in a focus is of particular interest in tip-enhanced scanning near-field optical microscopy.

Introduction

A single fluorescent molecule is among the smallest possible sensing devices one can think of. Exploiting their sensitivity to changes in the local environment, single dye molecules have been used as sensitive probes for dynamics in solids at low temperature and as markers in biological systems (Basché, 1997; Anon, 1999). The fluorescence rate of a single molecule is directly proportional to the strength of the squared electric field component parallel to its absorption dipole moment. Therefore, and because of its small extension, a single dye molecule is also an ideal probe for mapping confined optical fields. Scanning a single molecule with high spatial accuracy through a confined field distribution and recording the fluorescence count rate at each point yields an image pattern which is a map of the spatial distribution of the respective squared field component. Single-molecule images showing such effects were first noticed in aperture scanning near-field optical microscopy (SNOM) (Betzig & Chichester, 1993;

Correspondence: B. Hecht. Tel: +41 1 632 4392; fax: +41 1 632 1021; e-mail: hecht@phys.chem.ethz.ch

Veerman *et al.*, 1999). However, the method is not restricted to SNOM: distributions of confined fields for various kinds of scanning optical microscopies can be measured and compared quantitatively to simulations. This is a capability that may be of utmost importance for the future development of near-field optics. *Vice versa*, if the electric field distributions are precisely known a wealth of information can be inferred from microscopy images. We show that it is possible to determine precisely the orientation of molecules from their image pattern (Betzig & Chichester, 1993; Veerman *et al.*, 1999; Hollars & Dunn, 2000). A fundamental requirement for the determination of arbitrary molecular dipole orientations is that the three independent components of the optical excitation field are of comparable magnitude. By analysing single-molecule image patterns we find that a field distribution that satisfies this condition can be created by focusing a doughnut-shaped laser beam onto a dielectric/air interface using a high numerical aperture (NA) lens (Scully, 1990; Xie & Trautman, 1998; Sick *et al.*, 2000). Our results are of relevance in confocal microscopy of single molecules at interfaces and in tip-enhanced non-linear optical microscopy (Sanchez *et al.*, 1999). In the latter case, a strong longitudinal field component is necessary to create a strong field enhancement at a sharp metal tip (Martin & Girard, 1997; Sanchez *et al.*, 1999).

Theory

Ray optics

The theory for calculating the three-dimensional distribution of electromagnetic fields in a focus was developed by Richards & Wolf (1959) and is still of current interest (Bahlmann & Hell, 2000; Qabis *et al.*, 2000; Youngworth & Brown, 2000). Although a description by scalar wave theory is adequate when focusing with small numerical aperture lenses, the vectorial nature of light has to be taken into account for modelling the focusing process with high NA lenses. We consider the case of focusing linearly polarized light (*x*-direction) with a high NA lens. As
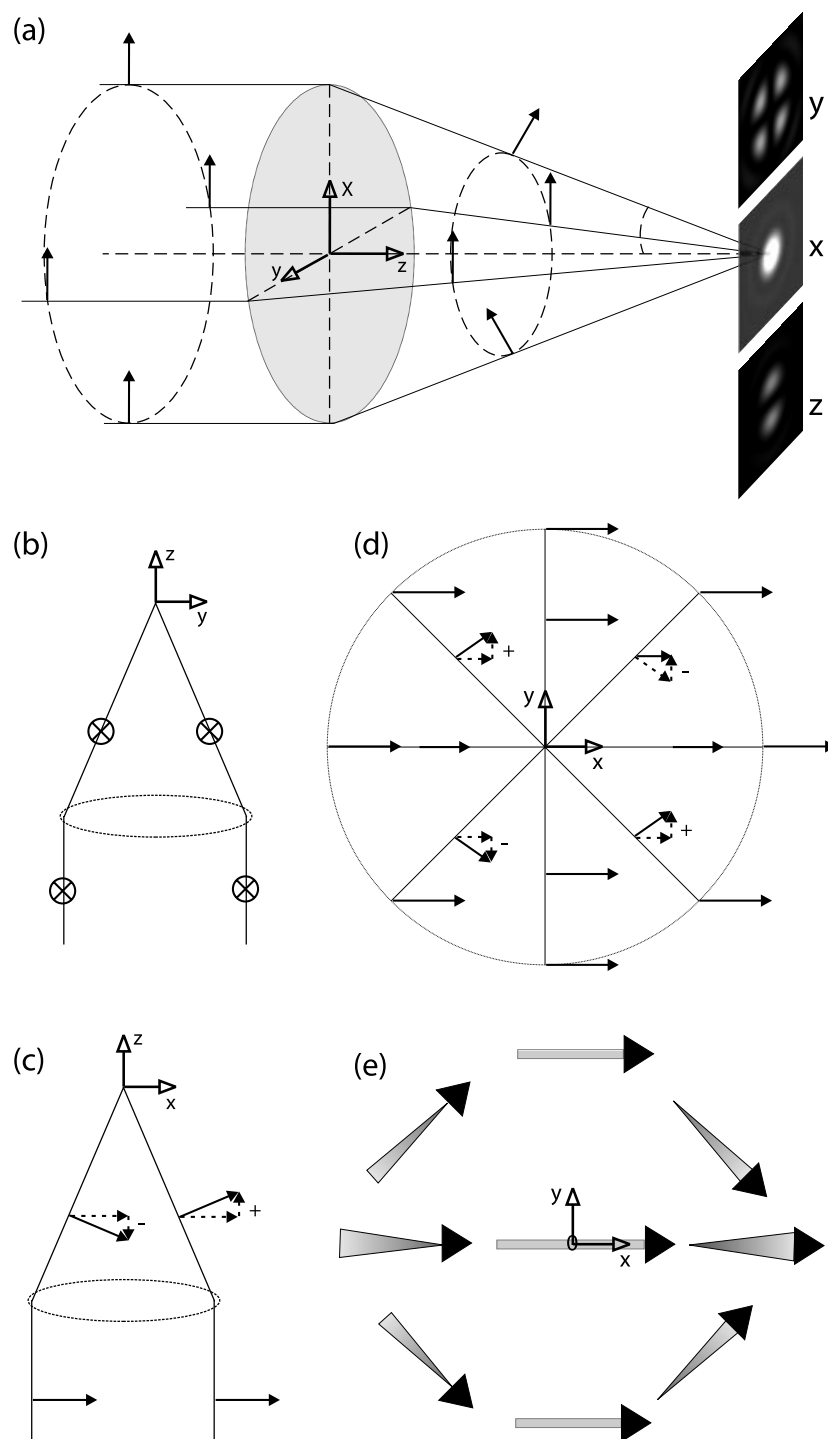
Fig. 1. (a) Image of the three-dimensional focusing optics. The *z*-axis is orientated along the optical axis and points in propagation direction of the light. The grey ellipse marks the position of the lens. The electric field vector is sketched by arrows. (b) Section along the yz-plane ($x = 0$). The orientation of the electric field vector points into the paper-plane ($\otimes$). (c) Section along the xz-plane ($y = 0$). The electric field vector is within the paper plane (arrow). (d) Projection onto the xy-plane as seen from the focus. The in-plane components of the electric field are represented (arrow). (e) Summary of the field distribution in the focal plane. The arrows depict the direction of the electric field vector at certain positions in the focal plane for a given instant in time. The pointed shape of the arrows illustrates the *z*-component of the field vector (adapted from representations of structural formulas in chemistry).
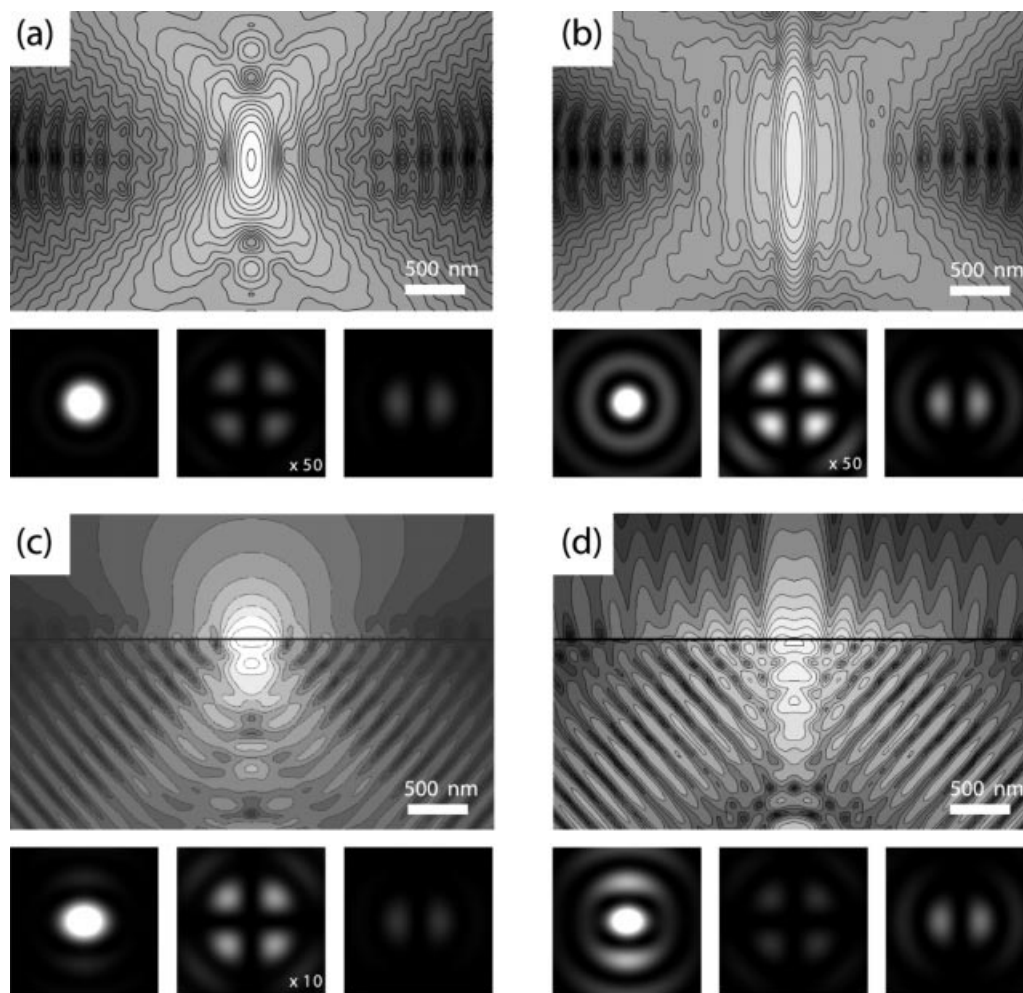
Fig. 2. Calculated distributions of squared electric field components in the focal region for different geometries as mentioned in the text: (a) homogeneous space, full illumination; (b) homogeneous space, annular illumination; (c) focus at the interface between glass (polymer) and air, full illumination; (d) focus at the interface between glass (polymer) and air, annular illumination. The large overview images show the squared total electric field in the xz-section through the geometrical focus (factor of two between adjacent lines). Each plot is accompanied by the respective plots of the squared x-, y- and z-components of the electric field in the focal plane (1 × 1 μm).

opposed to the scalar treatment, the vectorial description yields an electric (and magnetic) field in the focal region which also contains components perpendicular to the polarization direction (Richards & Wolf, 1959; Novotny et al., 1998; Bahlmann & Hell, 2000).

Figure 1(a) illustrates the geometry of the focusing problem in a ray optics picture. Although ray tracing is inadequate for mathematical modelling of the problem, it can rationalize the general shape and structure of the expected field distributions. The solid lines in Fig. 1(a) depict representative rays in the outer rim of the incident parallel beam. The electric field vector is oscillating along the x-direction; the arrows represent the field vector at a certain time at several positions along the beams. After focusing, all beams, apart from the one on the optical axis, are tilted. Consequently, the orientation of the electric field vector in

general rotates away from the pure x-orientation except for some classes of rays which will be discussed below. As a consequence, the field distribution in the focal region contains electric field components of all directions. On the right-hand side of Fig. 1(a) simulated distributions of the squared x-, y- and z-component of the electric field in the focal plane are shown (labelled by x, y, z, respectively). The x-pattern is a bright spot. The z-pattern consists of two equally intense lobes separated by a dark line along the y-axis. The y-pattern includes four equally intense lobes separated by a dark cross-shaped area orientated along the x- and y-axes. A qualitative explanation for the occurrence of these characteristic patterns is given in the following.

The pattern of the x-component of the electric field is created by superposition of the x-components of the fields in the focused rays. It results in a point-symmetric pattern with maximum in

the centre of the focus because symmetric rays there have the same phase and interfere constructively. Depending on the distance to the geometrical focus in the focal plane, rays have different optical pathways and therefore a finite phase difference. This results in less constructive interference and finally leads to destructive interference. Rays within the yz-plane (see Fig. 1(b)) only contribute to the x-component of the electric field. This explains the dark line along the y-axis in the y-pattern as well as in the z-pattern. Figure 1(c) visualizes the fact that, after focusing, rays in the xz-plane do not contain a y-component, which together with the dark line along the y-direction leads to the dark cross in the y-pattern.

Rays in the xz-plane in general do acquire a z-component of the electric field due to the tilting of the rays. Figure 1(c) shows that symmetric off-axis rays have z-components of equal values but opposite signs. Thus, superposition in the focal plane leads to a vanishing z-component on the y-axis. At positions away from the y-axis the resulting field contains a non-vanishing z-component because in this cases the two interfering rays have a finite pathway difference at the point of superposition. These considerations provide a qualitative explanation for the shape of the distribution of the z-component of the electric field, which comprises two equally intense and symmetric lobes separated by a dark line on the y-axis.

Whereas Fig. 1(c) explains the existence of the dark cross in the y-pattern, Fig. 1(d) illustrates why the focal field contains y-components at all. The figure shows a projection of Fig. 1(a) as seen from the focus. The eight straight lines symbolize rays at the rim of the beam which converge towards the focus. Rays on the x- or y-axis have no y-component, whereas all other off-axis beams contain a small y-component due to focusing (Richards & Wolf, 1959). The larger the aperture angle of the ray, the larger is its electric field y-component. The sign of the y-components alternate from quadrant to quadrant, as shown in Fig. 1(d). Accordingly, superposition actually leads to non-vanishing amplitudes only in the corner areas.

Figure 1(e) summarizes the field distribution in the focal plane. The arrows depict the direction of the electric field vector at certain positions in the focal plane for a given instant in time. The pointed shape of the arrows illustrates the z-component of the field vector (adopted from representations of structural formulae in chemistry). This pictorial description of the field distribution provides an impression of the type of image pattern obtained for arbitrarily oriented dye molecules.

Field simulations

From the above considerations it is clear that rays with high semi-aperture angles α have particularly large y- and z-components of the focal electric field. Therefore, the relative importance of perpendicular field components with respect to

the polarization can be enhanced as compared to the parallel component if the inner part of the beam is blocked (annular illumination) (Scully, 1990). In order to confirm this, we have calculated the electric field in the vicinity of the geometric focus for the following four geometries in order to assess the influence of different experimental parameters (see Fig. 2): (a) homogeneous medium with full illumination, (b) homogeneous medium with annular illumination, (c) focus at a dielectric interface with full illumination, and (d) focus at a dielectric interface with annular illumination.

Focal field calculations for a homogeneous medium with full and annular illumination have been performed using an integral solution of the focal field (Richards & Wolf, 1959). It contains diffraction integrals that were evaluated numerically using a series expansion (Kant, 1993). In the case of the presence of an interface the multiple multipole method (Hafner, 1990) can be used to determine the electromagnetic field distribution in the focal area. In this approach the scattered fields at the interface are treated as an analytic series expansion of multipoles distributed along the interface. The coefficients in the expansion are determined numerically to comply with the boundary conditions at discrete points on the interface. Figure 2 shows the squared total field ($|\vec{E}|^2$) in the xz-plane (logarithmic scale) for the geometries (a), (b), (c), and (d) as well as the respective squared x, y and z electric field components in the focal plane. In the presence of the interface (Figs 2(c) and (d)), rays undergoing total internal reflection lead to a (weak) standing wave pattern in the higher index medium. Annular illumination slightly reduces the spot size (Wilson & Sheppard, 1984). However, this reduction is at the expense of more pronounced sidelobes. In the case of annular illumination the focal spot splits above the interface into two spots aligned along the direction of polarization and separated by $\approx$ 200 nm. It is remarkable that the relative strength of the field components changes strongly for the different geometries (in scheme (d) the squared y-component is about 50 times stronger than in scheme (a)), whereas the shape of their distribution in the focal plane is nearly unaffected by the different geometries.

Fluorescence

A single dye molecule is very well suited to map the distribution of field components with nanometre-scale accuracy and resolution because it has an absorption cross-section in the 10^{-1} nm to nm-range and its fluorescence rate $R(\vec{r})$ is given by (Plakhotnik *et al.*, 1997)

$$R(\vec{r}) = c|\hat{d}\cdot\vec{E}(\vec{r})|^2 \qquad (1)$$

Here, $\hat{d}$ is the unit vector along the absorption dipole moment of the molecule, $\vec{E}(\vec{r})$ is the electric field vector at the position of the molecule, $\vec{r}$ and c is a constant. The fluorescence rate is directly proportional to the squared field
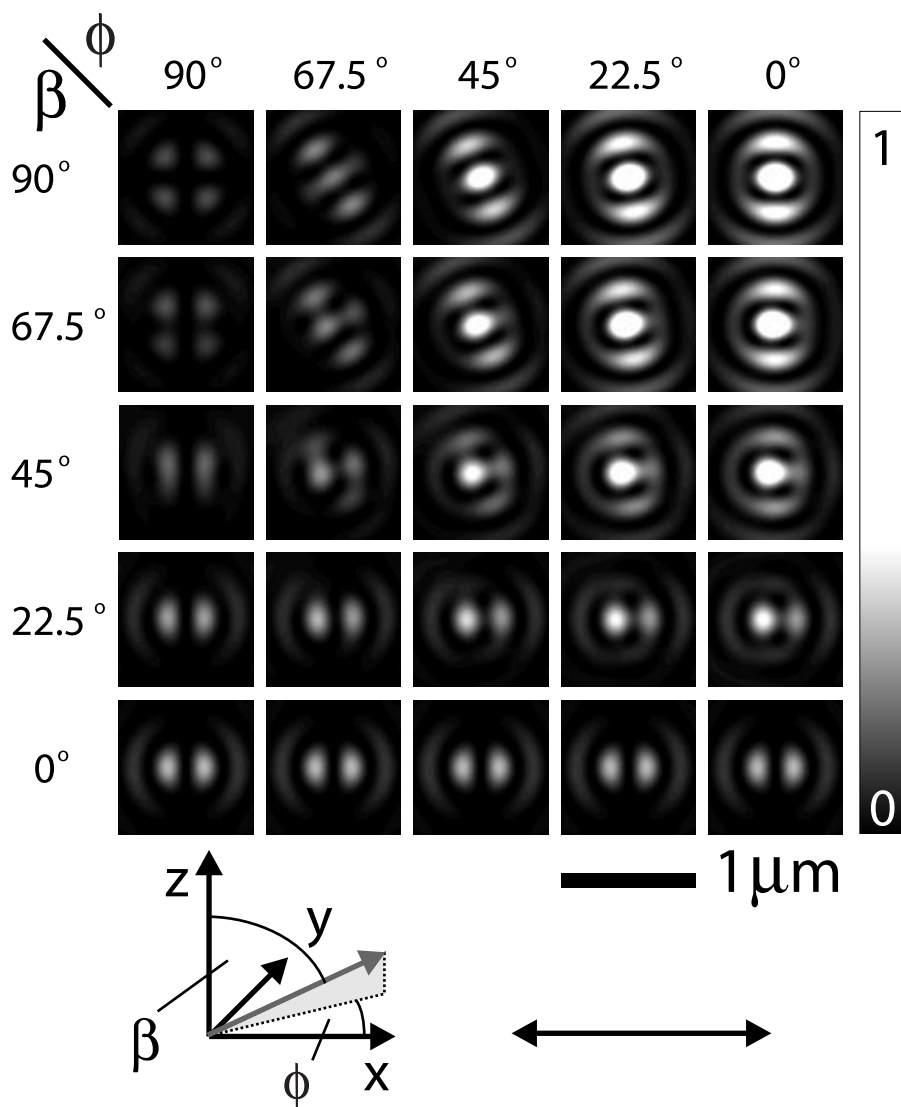
Fig. 3. Single-molecule image patterns calculated from the field distribution 5 nm below the interface according to Eq. (1) for an array of dipole orientations. The *xyz* coordinate system indicates the definition of the dipole orientation angles β and ϕ with respect to the excitation polarization (double arrow).

component parallel to the absorption dipole vector. The above relation is valid as long as the excitation intensity is far from saturation. Once the electric field distribution is known it is possible to calculate image patterns of single molecules according to Eq. (1). In Fig. 3 the expected image patterns for molecular dipoles of varying orientations according to Eq. (1) are displayed. All patterns obey the same contrast settings (scale bar on the right). The patterns change gradually as the dipole is rotated with respect to the direction of polarization. In the corners of the matrix the three pure image patterns (*x*, *y* and *z* orientation) are recovered. Patterns for other orientations, i.e. for negative angles, than those displayed can be obtained by simple symmetry considerations.

Experimental section

Set-up

Figure 4 shows the set-up used in the present study. Light from an Ar$^+$ laser with a wavelength of 514 nm is coupled into a single mode fibre. The polarization of the light after exiting the fibre is controlled by exerting variable stress over a fixed length, stripped section of the fibre by means of a commercial device (L.O.T., Polarite, Darmstadt, Germany). Linear polarization is achieved by varying the amount and direction of the applied stress. The light is collimated by a lens (L1, $f = 50$ mm) and reflected via a dichroic mirror onto the 6.3 mm diameter entrance aperture of an immersion oil microscope objective
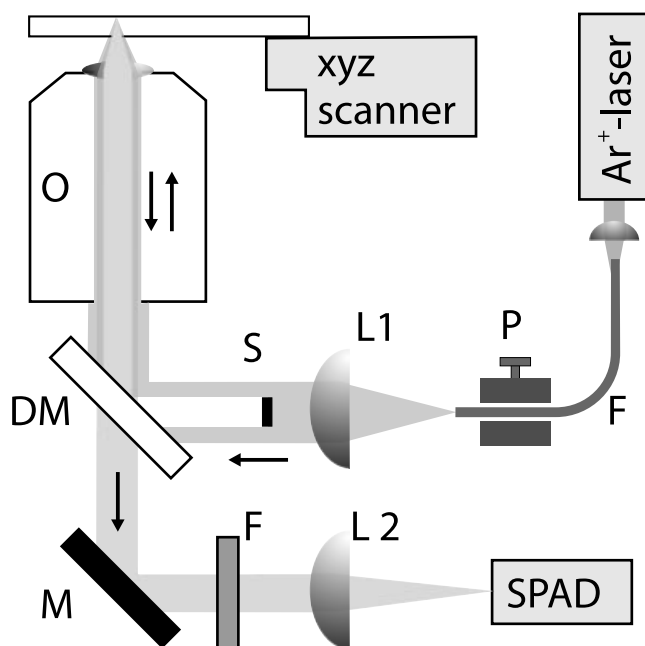
Fig. 4. Set-up for annular illumination scanning confocal optical microscopy. L1: collimation lens ($f = 50$ mm), O: microscope objective (Leica, PL Fluotar, $\times$ 100, 1.3 NA, ∞), DM: dichroic mirror, M: mirror, F: holographic notch filter, L2: focusing lens ($f = 300$ mm), SPAD: single photon counting avalanche photodiode (EG & G SPCM 200), S: beam blocker (3 mm diam.), P: polarization controller (L.O.T., Polarite), F: single mode fibre.

(Leica, PL Fluotar, $\times$ 100, 1.3 NA, ∞). For annular illumination a circular on-axis beam-stop with a diameter of 3 mm is built into the illumination path, which blocks the central part from the beam before being reflected at the dichroic mirror and entering the microscope objective. The resulting doughnut-shaped beam is focused to a diffraction-limited spot onto the thin sample on top of a cover glass. Opening angles between $38°$ and $58°$ contribute to the field distribution in the focus. The full angular range of fluorescence, collected by the same objective, now passes the dichroic mirror and a holographic notch filter and is finally focused via a lens (L2, $f = 300$ mm) to a 100 μm spot onto the active area of a photon-counting avalanche photodiode. The 200 μm diameter active area serves as a confocal pinhole. The size of the back-projected image of the active area into the focal plane is about 1 μm in diameter. Single-molecule fluorescence images were recorded at excitation intensities far from saturation by raster scanning the sample through the focus using a linearized x-y-z piezo scan table and recording the number of counts for each pixel.

Sample preparation

Samples were prepared by spin-casting (9600 rev min^{-1}) of a 10 μL droplet from a solution of polymethylmetacrylate (PMMA) in toluene that also contains the dye

1,1′-dioctadecyl-3,3,3′,3′-tetramethylindocarbocyanine (DiI) in a concentration of 10^{-9} M onto standard glass cover slips. Before that the cover slips were cleaned by baking them at 510 °C for 6 h. The difference in the refractive indices of PMMA and glass is negligible. The only relevant step in the dielectric constant occurs at the PMMA/air boundary. Atomic force microscopy of the polymer films revealed a smooth surface and a thickness of about 30 nm.

Results and discussion

We restrict our discussion to the comparison of experimental results and theory in the case of a dielectric interface in combination with annular illumination [case (d)]. Figure 5 shows single-molecule fluorescence images of a dye-doped polymer film. The orientation of the electric field vector of the incident light before focusing is indicated by the arrows in the images. Various spot shapes can be observed. Patterns corresponding to molecules with x-, y- z-orientation are marked with x, y and z, respectively. The patterns are generated by the fluorescence emission of single molecules because (i) some of the patterns are truncated caused by digital photo-bleaching during line-by-line image acquisition (the images in the top row were recorded from left to right, the images in the bottom row from bottom to top), (ii) some patterns exhibit intermittent dark spots due to excursions to a dark state, e.g. the triplet state, and (iii) the patterns are in agreement with expected fluorescence images of a single point-like dipole.

The two images in the top row of Figs 5(a) and (c), and bottom row (b) and (d), each show the same area with the excitation polarization turned by 90°. The patterns therefore appear at the same positions in the images of the left and right column and can be assigned to the same dye molecule being fixed in the PMMA matrix, respectively. The different appearance of the same molecule can be explained by the changed field distribution in the focal region due to the rotated polarization of the incidence light. This is nicely illustrated by the two molecules which are marked with y in Fig. 5(a) and with x in Fig. 5(c). Both show in Fig. 5(a) a pattern which is consistent with a molecule mapping the squared y-component of the electric field distribution in the focus. We therefore conclude that the molecular absorption dipole lies in the focal plane and perpendicular to the direction of polarization. In image Fig. 5(c) the polarization is rotated by 90° and is thus parallel to the orientation of these two molecules. Accordingly, they now map the x-component of the focal field distribution. The pattern marked by z remains unchanged in Figs 5(b) and (d); however, its orientation follows the direction of polarization.

According to this consideration the three-dimensional orientation of each molecule in the imaged area can be determined from a single scanning image by comparing the fluorescence patterns with the calculated maps of squared
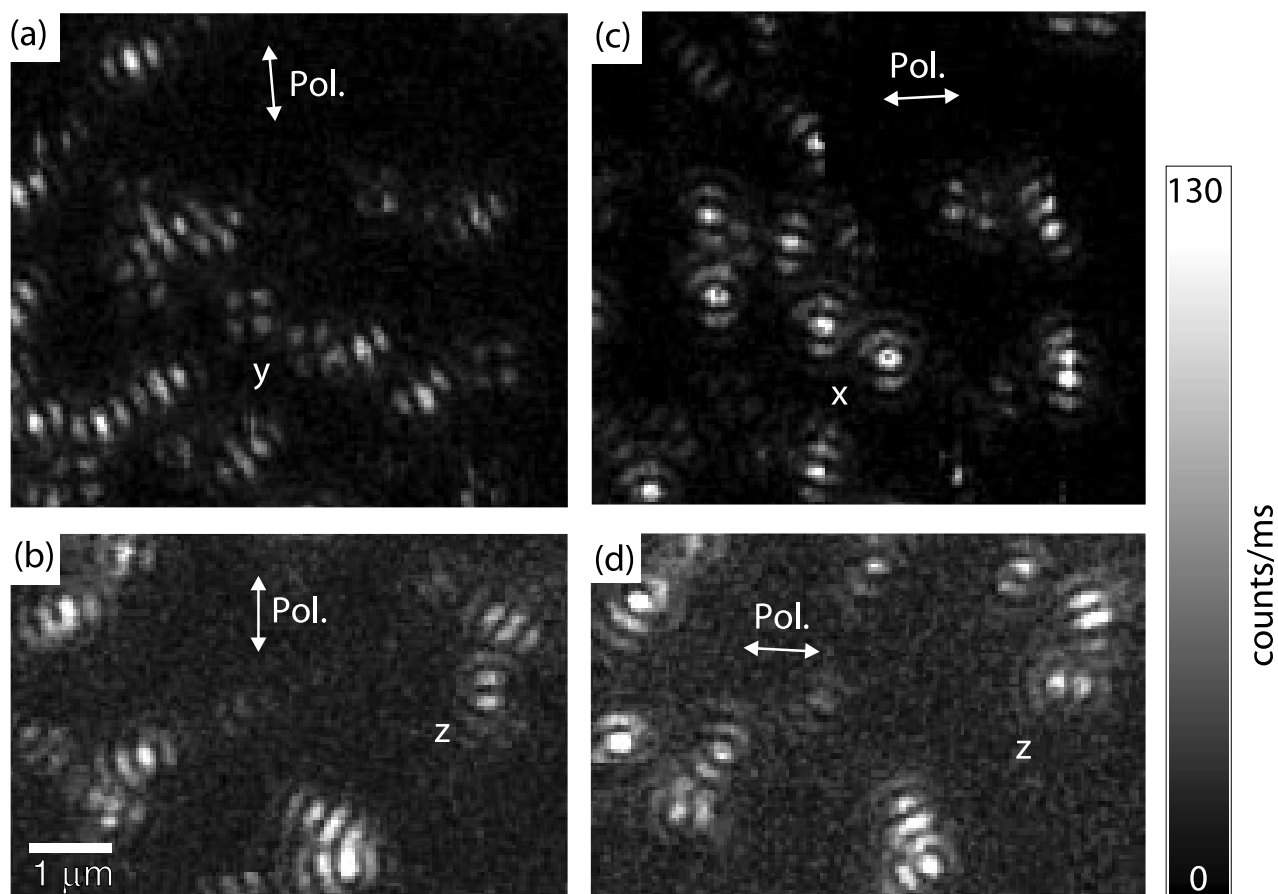
Fig. 5. Confocal single molecule fluorescence image of DiI in a thin film of PMMA obtained with linearly polarized (arrow), annular illumination. Characteristic patterns are labelled by *x*, *y* and *z*. They result from molecules that map the squared *x*-, *y*- and *z*-components of the electric field in the focus, respectively.

field components for different orientations, as displayed in Fig. 3. The reliability of orientation determination using this method is discussed in more detail elsewhere (Sick *et al.*, 2000).

At this point we want to compare measured and calculated field distributions. For this purpose it is most illustrative to compare the measured *x*-, *y*- and *z*-patterns with the corresponding simulations. Figure 6 shows the comparison between measurement and simulation. The images in row A are measured image patterns, row B shows the respective calculated maps of the squared *x*-*y*- and *z*-field components in the focal plane (column *x*, *y* and *z*). The measured as well as the calculated images have a size of 1×1 µm, with the origin in the centre of the patterns. Either two (in the case of the *x*- and *z*-pattern) or three characteristic line cuts (in the case of the *y*-pattern) were taken at the same positions in the measured and calculated images. The cuts taken from the measured images and calculated patterns are indicated by solid and dashed lines, respectively. The resulting intensity profiles were normalized. The top and the bottom row shows the horizontal

sections and the vertical and diagonal sections, respectively. Experiments and theory are compared without adjustable parameters apart from normalization.

A first glance at the profiles in Figure 6 reveals a good agreement between measurements and calculations, regarding the general curve shape as well as the size, position, and relative intensities of main and side peaks. The vertical sections in the observed and calculated *x*-pattern match nearly perfectly. The horizontal sections in the *x*-patterns show that the measured width of the peaks are slightly broader (14%) than the calculated peaks. The intensity of the side peaks is 24% larger in the calculated pattern than in the measured pattern. The positions of the side peaks match perfectly. In case of the *y*-pattern, all profiles show a very good agreement with respect of relative intensities of main and side peaks. In the upper right corner the side lobe of another molecule overlaps with the side lobe of the investigated pattern, which causes larger intensities in this area (factor of 2). The horizontal section in the *z*-patterns reveals a wider peak-width (14%) in the measurement than in the calculation, and the measured side-lobes are more
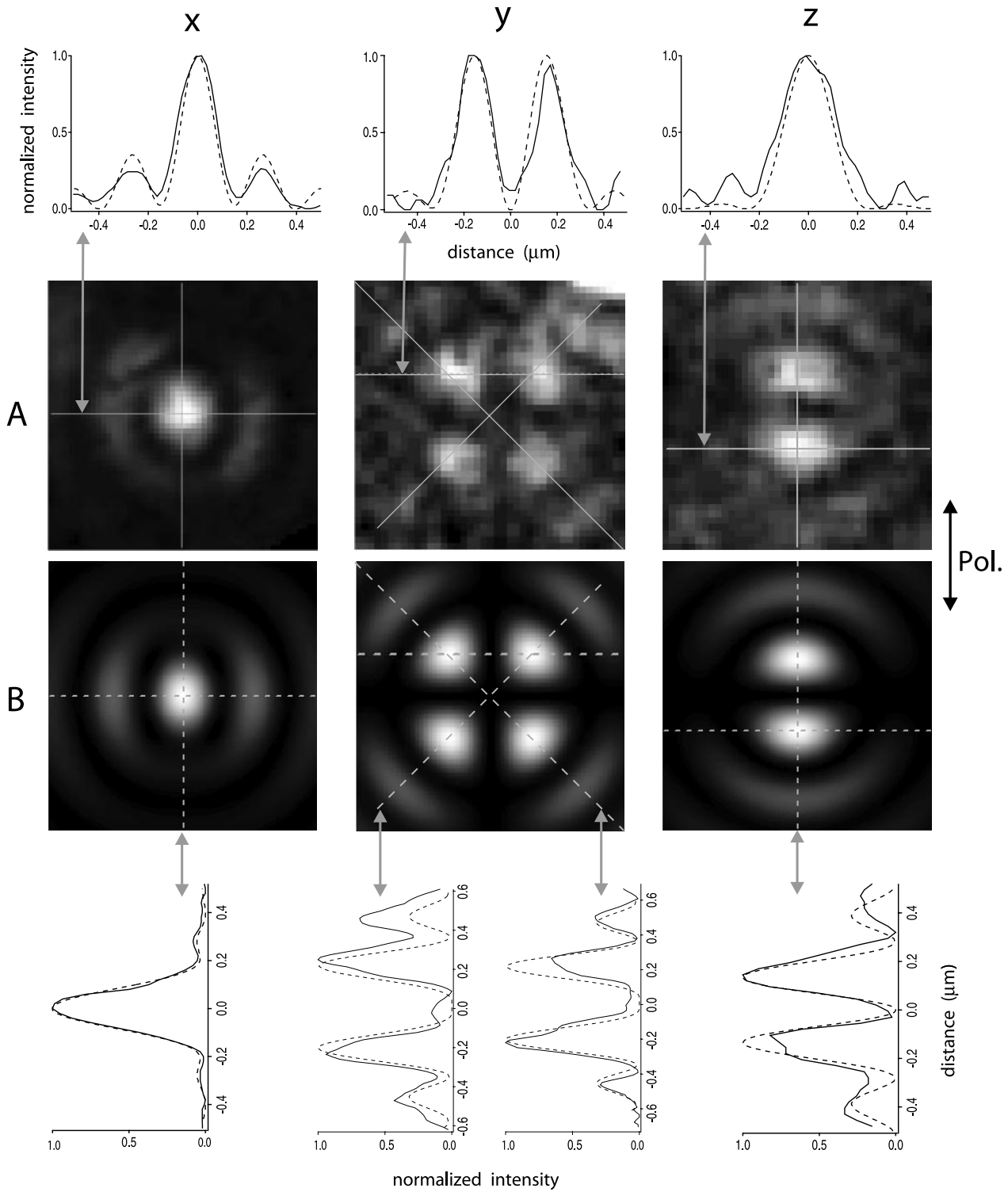
Fig. 6. Comparison of measured and calculated field maps. In columns: field-maps in the focal plane of the squared *x*-, *y*- and *z*-component indicated with *x*, *y* and *z*. The top row shows intensity profiles of the horizontal sections of the measurements (solid curves) and simulations (dashed curves). Row A: measured field maps, Row B: calculated field maps. Bottom row: intensity profiles of vertical and diagonal sections of the measured data (solid curves) and simulations (dashed curves).

pronounced. This is similar to the case of the x-pattern (x, A). The intensity profiles of the vertical section match very well even though the molecule shows blinking during the image acquisition. Other conspicuous features in the measured pattern are some black or rather dark pixels within the patterns. They result from excursions to a dark state of fluorescence (e.g. a triplet state). Black pixels turn up if the off-time exceeds the integration time of 1 ms per pixel and pixels with reduced intensity appear for shorter dark state lifetimes. Additionally, intermediate intensities are caused by interpolation between two adjacent pixels, which was the only image processing performed. Furthermore, there is a certain influence of shot noise in the measured data.

Conclusions

On the basis of this striking agreement we conclude that the measured field distributions confirm the model of the focusing process with high numerical apertures. Single molecules can accordingly be used to quantitatively map the spatial distribution of confined optical fields with great accuracy. The remaining deviations between simulation and data in the present study are partly caused by blinking and shot noise. Both sources of errors can be decreased by increasing the integration time. However, an increased integration time decreases the time resolution and increases the risk of photo-bleaching during image acquisition. For long integration times orientational diffusion can blur the observed patterns. Apart from these sources of errors inherent to the method there are actually small differences between the model and the actual experimental configuration. For example, the incident light may be not perfectly linearly polarized (typical depolarization between 10^{-2} and 10^{-3}). Also the model assumption of an incident plane wave is not perfectly fulfilled by a laser-beam with Gaussian profile even if the entrance aperture is over-illuminated.

Acknowledgements

References

Anon. (1999) Frontiers in Chemistry, Science Special Issue. Single Molecules, *Science* **283**.

Bahlmann, K. & Hell, S.W. (2000) Depolarization by high aperture focusing. *Appl. Phys. Lett.* **77**, 612–614.

Basché, T., Moerner, W.E., Orrit, M. & Wild, U.P. (1997) *Single-Molecule Optical Detection, Imaging and Spectroscopy*, VCH, Weinheim.

Betzig, E. & Chichester, R.J. (1993) Single molecules observed by near-field scanning optical microscopy. *Science*, **262**, 1422–1425.

Hafner, C. (1990) *The Generalized Multiple Multipole Technique for Computational Electrodynamics*. Artech, Boston, Mass.

Hollars, C.W. & Dunn, R.C. (2000) Probing single molecule orientations in model lipid membranes with near-field scanning optical microscopy. *J. Chem. Phys.* **112**, 7822–7830.

Kant, R. (1993) An analytical solution of vector diffraction for focusing Optical systems. *J. Mod. Opt.* **40**, 337–347.

Martin, O.J.F. & Girard, C. (1997) Controlling and tuning strong optical field gradients at a local probe microscope tip apex. *Appl. Phys. Lett.* **70**, 705–707.

Novotny, L., Sanchez, E.J. & Xie, X.S. (1998) Near-field optical imaging using metal tips illuminated by higher-order Hermite-Gaussian beams. *Ultramicroscopy*, **71**, 21–29.

Plakhotnik, T., Donley, E.A. & Wild, U.P. (1997) Single-molecule spectroscopy. *Annu. Rev. Phys. Chem.* **48**, 181–212.

Qabis, S., Dorn, R., Eberler, M., Glöckl, O. & Leuchs, G. (2000) Focusing light to a tighter spot. *Opt. Commun.* **179**, 1–6.

Richards, B. & Wolf, E. (1959) Electromagnetic diffraction in optical systems. II. Structure of the image field in an aplanatic system. *Proc. R. Soc. London A*, **253**, 358–379.

Sanchez, E.J., Novotny, L. & Xie, X.S. (1999) Near-field fluorescence microscopy based on two-photon excitation with metal tips. *Phys. Rev. Lett.* **82**, 4014–4017.

Scully, M.O. (1990) A simple laser linac. *Appl. Phys. B*, **51**, 238–241.

Sick, B., Hecht, B. & Novotny, L. (2000) Orientational imaging of single molecules by annular illumination, *Phys. Rev. Lett.* **85**, 4482-4485.

Veerman, J.A., Garcia-Parajo, M.F., Kuipers, L. & Van Hulst, N.F. (1999) Single molecule mapping of the optical field distribution of probes for near-field microscopy. *J. Microsc.* **194**, 477–482.

Wilson, T. & Sheppard, C.J.R. (1984) *Theory and Practice of Scanning Optical Microscopy*, Academic Press, London.

Xie, X.S. & Trautman, J.K. (1998) Optical studies of single molecules at room temperature. *Annu. Rev. Phys. Chem.* **49**, 441–480.

Youngworth, K.S. & Brown, T.G. (2000) Focusing of high numerical aperture cylindrical-vector beams. *Optics Express*, **7**, 77–87.